Towards Balance Recovery Control for Lower Body Exoskeleton Robots with Variable Stiffness Actuators: Spring-Loaded Flywheel Model

Corinne Doppmann, Barkan Ugurlu, Masashi Hamaya, Tatsuya Teramae, Tomoyuki Noda, and Jun Morimoto

***Abstract*— This paper presents a biologically-inspired real-time balance recovery control strategy that is applied to a lower body exoskeleton with variable physical stiffness actuators at its ankle joints. For this purpose, a torsional spring-loaded flywheel model is presented to encapsulate both approximated angular momentum and variable physical stiffness, which are crucial parameters in describing the postural balance. In particular, the incorporation of physical compliance enables us to provide three main contributions: i) A mathematical formulation is developed to express the relation between the dynamic balance criterion ZMP and the physical ankle joint stiffness. Therefore, balancing control can be interpreted in terms of ankle joint stiffness regulation. ii) *'Variable physical'* stiffness is utilized in the bipedal robot balance control task for the first time in the literature, to the authors' knowledge. iii) The variable physical stiffness strategy is compared with the optimal constant stiffness strategy by conducting experiments on our exoskeleton robot. The results indicate that the proposed method provides a favorable balancing control performance to cope with unperceived perturbations, in terms of center of mass position regulation, ZMP error and mechanical power.**

I. Introduction

Starting with Vukobratovic's work [1], numerous lower body exoskeletons have been developed for various applications, ranging from power augmentation [2] and robot-aided rehabilitation [3] to paraplegia walking support [4]–[6] and gait assistance [7]–[10]. An exhaustive review on lower limb rehabilitation devices is provided in [11].

In exoskeleton actuators, the incorporation of physical compliance is of importance when it comes to dependability, low mechanical impedance, locomotion efficiency, inherent safety and enhanced environmental interaction capabilities [11]–[13]. Though the software-controlled active compliance schemes can enhance environmental interaction capabilities [6]–[8], the rest of the listed benefits may not be acquired due to fundamental open-loop characteristics of actuators with low compliance [13]. Consequently, several exoskeletons are powered via passively compliant actuators [10], [14]–[16].

In this connection, compliant systems with VSAs (Variable Stiffness Actuator) possess superior characteristics compared to their unadaptable stiffness counterparts [17]. This is also evident in biological systems; for instance, the central nervous system modulates muscle impedance to address adaptive control during daily tasks [18], resulting in improved robustness and efficiency [19]–[21]. In order to emulate such enhanced characteristics in robotic systems, a wide range of VSA modules have been developed [17].

Despite the extraordinary cumulative effort in VSA development [17], adjustable stiffness property has not been exploited thoroughly in legged robotics, especially in exoskeleton control. Robots that are equipped with VSAs were manufactured (such as [16]); however, variable stiffness has not been vastly exploited in the context of legged robot control. Hence, this paper aims to contribute in this direction.

As hypothesized in [18]–[20], the stiffness modulation can be interpreted by means of a control action to cope with external disturbances. In particular, ankle stiffness regulation in elderly people is observed to be of importance during unperceived perturbation of standing motion [20]. Inspired by the findings in [20], we propose a real-time balance recovery control strategy for our lower body exoskeleton in which the ankle stiffness is modulated to handle unperceived perturbations. Our lower body exoskeleton is powered via PAMs (Pneumatic Artificial Muscle) and its ankle joints are driven antagonistically. This allows the real-time simultaneous control of both position and physical stiffness at its ankle joints [22]. Considering these factors, this paper presents three main contributions:

1) *'Variable physical'* stiffness is utilized in the bipedal robot balance control task for the first time in the literature, to the authors' knowledge. Passively compliant exoskeletons and humanoids with unadjustable physical stiffness [10], [23], [24], and software-controlled virtually compliant systems [25]–[27] demonstrated balancing control; however, the exploitation of variable physical stiffness has not been investigated so far. Therefore, this is the first application of variable physical stiffness for the bipedal system balance control task.

2) A torsional spring-loaded flywheel model is introduced by properly combining the concepts in [27] and [28]. In doing so, the dynamic balance criterion, Zero Moment Point (ZMP), is mathematically correlated with the variable physical stiffness. The model comprises both the physical stiffness and the approximated angular momentum of the system, which are of importance in describing postural balancing.

3) The variable stiffness strategy is compared with the optimal constant stiffness strategy [24] via experiments on the real robot, in terms of CoM (Center of Mass) position regulation, induced ZMP error, reaction force, mechanical power and air mass consumption.

This paper is organized as follows. The lower body ex-

The authors are with the Department of Brain Robot Interface, Computational Neuroscience Laboratories, Advanced Telecommunications Research Institute International (ATR), 619-0288 Kyoto, Japan. C. Doppmann is also with the Department of Microengineering, Ecole Polytechnique Federale de Lausanne (EPFL), 1015 Lausanne, Switzerland. B. Ugurlu is also with the Department of Mechanical Engineering, Ozyegin University, 34794 Istanbul, Turkey. M. Hamaya is also with the Graduate School of Frontier Biosciences, Osaka University, 565-0871 Osaka, Japan. e-mail: barkan.ugurlu@ozyegin.edu.tr; xmorimo@atr.jp

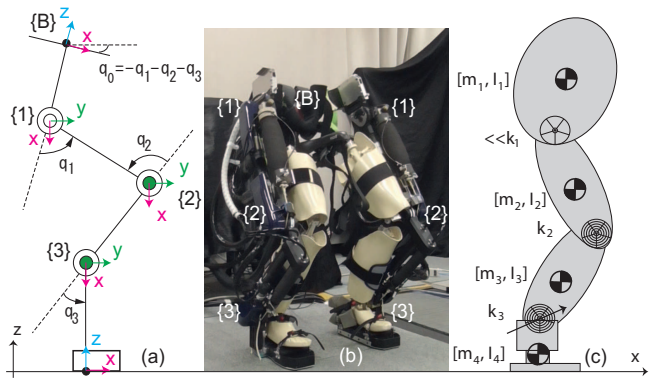

Fig. 1. a) Joint frames of XoR in the sagittal plane. b) The actual robot, XoR, while standing on its own with a dummy. c) Multi-DoF representation of XoR in the sagittal plane. Knee and ankle joints are passively compliant. The arrow on the ankle joint indicates the stiffness variability.

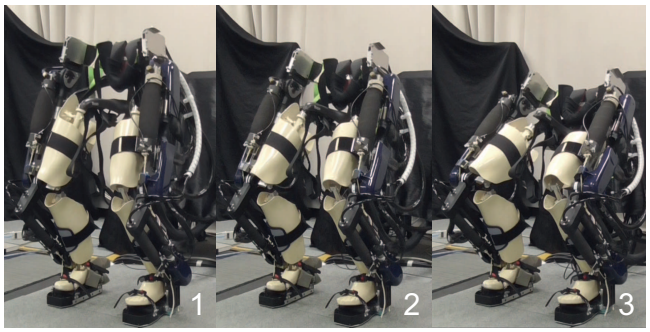

Fig. 2. The lower body exoskeleton robot XoR, performing self-balanced squatting motion with a dummy mannequin inside. The PAM-powered robot demonstrates its feasible position control capabilities [22].

oskeleton platform we used in the experiments is introduced in section II. The proposed real-time balance recovery control is explained in section III. Experiment results are discussed in section IV, and the paper is concluded in section V.

II. XoR: Lower Body Exoskeleton

A bipedal lower body exoskeleton, named XoR, was developed at the BRI-Computational Neuroscience Labs. of ATR, to serve as a testbed in our robot-aided rehabilitation, sensorimotor learning and neurophysiology studies [23]. It has 3 active DoFs (Degrees of Freedom) in each leg (6 in total) with hip-knee-ankle configuration, through flexion/extension. Hence, it can perform two-legged squatting and balancing with no support/tethering mechanism, although its motion is constrained in the x-z plane. Fig. 1 displays the actual robot and its joint frames. Its mechanical specifications are briefly given in Table I. Fig. 2 shows three snapshots from the self-balanced squatting experiments with a dummy mannequin.

The main power source in XoR is PAMs (Pneumatic Artificial Muscle). They are chosen because of their high power-to-weight ratio and physical compliance [17]. Both ankle joints are driven antagonistically via a pair of PAM units (Festo MAS-10) through flexion/extension. Knee joints are driven by single PAM units (Festo MAS-40) through flexion.

TABLE I
Mechanical Specifications of XoR Lower Body

Hip - Knee length:	390 [mm]
Knee - Ankle length:	380 [mm]
Ankle - sole length:	140 [mm]
Total Weight	22.2 [kg]

Since the current version is mainly designed for the tasks with no stepping involved, hip joints require the minimum amount of torque. Thus they are actuated via low power electrical motors (Maxon, EC-4 pole). This *hybrid* actuation approach is considered so as to satisfy dimensional and weight requirements while achieving physical compliance and high joint torque output at the ankle and knee joints.

Antagonistically driven ankle joints allow the simultaneous control of position (q_3) and variable physical stiffness (k_3) [22]. As knee joints are driven via single PAM units, we can control its position (q_2); however, its stiffness (k_2) is not controllable. Using the forward stiffness model and torque measurements, we can estimate (observe) the changes in knee joint stiffness [22]. Motor-powered hip joints allow position control (q_1) only. They theoretically possess no physical compliance and we assume this holds true in practice.

The current version of XoR was primarily designed to generate motions in the sagittal plane, for instance, sit-down and stand-down rehabilitation [3], squatting and active balancing. Therefore, this paper focuses on sagittal plane motions in the x-z plane, in which the legs are moved in a synchronized manner. Considering these facts, the robot is modeled as a 4-link 3-DoF system with a variable stiffness actuator at the ankle, a passively compliant actuator at the knee, and a stiff actuator at the hip, as displayed in Fig. 1(c). As robot legs move synchronously, the ankle joint stiffness in this model is equally distributed to the left and right ankle joints of XoR. This approach was practically confirmed to be viable for a passively compliant biped [29].

III. Balance Control by Varying Ankle Stiffness

A. Torsional Spring-Loaded Flywheel Model

Explicit mathematical formulation of dynamic equilibrium for a multi-link passively compliant robot is usually challenging. Therefore, abstracted models are often used [24]–[28]. In this study, we use the torsional-spring loaded flywheel model which combines the concepts introduced in [27] and [28], see Fig. 3. In this model, the robot is considered as a flywheel disk with the rotational inertia of I_f and the total mass of m. It is in contact with the floor through a telescopic leg and a rectangular foot. The leg length l and the angle with the vertical z-axis α describes the CoM position in polar coordinates. A torsional spring with a variable stiffness of k_f connects the leg and the vertical z-axis. The spring is in the rest state when $\alpha = \alpha_0$.

This model is chosen due to the fact that it encapsulates two important characteristics of postural balancing: i) It can characterize the approximated angular momentum, unlike point mass pendulums. Although the actual rotational inertia

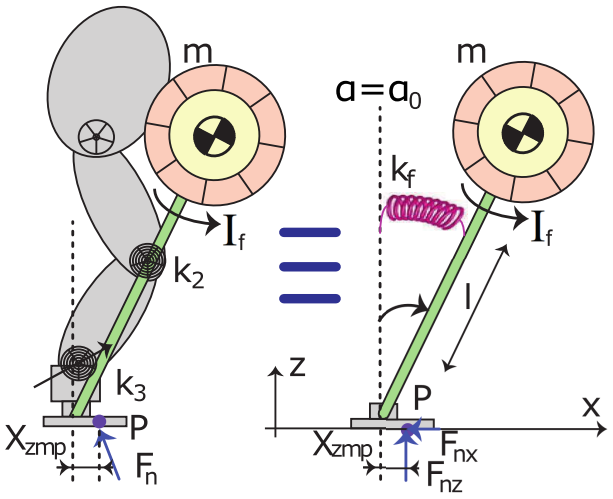

Fig. 3. Torsional spring loaded flywheel model. The model captures the approximated angular momentum and physical compliance of the robot.

of the system is joint state-dependent, we can capture a value of I_f given the CAD data and motion range [28]. ii) It can represent the physical compliance of the system through the use of k_f. The flywheel stiffness k_f can then be mapped to ankle joint stiffness k_3, as described in the next subsection.

In order to formulate the relation between ZMP and physical stiffness, we use Lagrangian mechanics. CoM position in polar coordinates (l, α) are the generalized coordinates.

$$T = \frac{1}{2}m\left(\dot{l}^2 + l^2\dot{\alpha}^2\right) + \frac{1}{2}I_f\dot{\alpha}^2 \quad (1)$$

$$U = \frac{1}{2}k_f\left(\alpha - \alpha_0\right)^2 + mgl\cos\alpha \quad (2)$$

$$D = \frac{1}{2}b_f\dot{\alpha}^2 \quad (3)$$

In (1)-(3), T, U and D symbolize total kinetic energy, total potential energy and Rayleigh's dissipation function. b_f accounts for the frictional and other damping effects through α. When the Lagrangian is calculated as $L = T - U$, equations of motion can be derived as follows.

$$\frac{d}{dt}\frac{\partial L}{\partial \dot{l}} - \frac{\partial L}{\partial l} + \frac{\partial D}{\partial \dot{l}} = F_n \quad (4)$$

$$\frac{d}{dt}\frac{\partial L}{\partial \dot{\alpha}} - \frac{\partial L}{\partial \alpha} + \frac{\partial D}{\partial \dot{\alpha}} = M_n \quad (5)$$

F_n and M_n are the external force and moment acting on the system. When considering the postural balance, only eq. (5) is relevant, as the external moment in the sagittal plane can be expressed in terms of x-axis ZMP (X_{zmp}) and z-axis external force (F_{nz}); see Fig. 3.

$$M_n = F_{nz}X_{zmp} \quad (6)$$

Combining (5) and (6), the equation of motion is derived.

$$\begin{aligned} F_{nz}X_{zmp} &= (ml^2 + I_f)\ddot{\alpha} + 2ml\dot{l}\dot{\alpha} + k_f(\alpha - \alpha_0) \\ &+ b_f\dot{\alpha} - mgl\sin\alpha \end{aligned} \quad (7)$$

In (7), $I_f\ddot{\alpha}$ corresponds to the rate change of angular momentum that is associated with the rotational inertia.

B. Mapping from Flywheel Stiffness to Ankle Joint Stiffness

Equation (7) expresses the mathematical relation between the dynamic balance criterion ZMP (X_{zmp}) and flywheel stiffness (k_f), in addition to other terms. Thus, mapping from flywheel stiffness (k_f) to ankle joint stiffness (k_3) is required to construct the mathematical relation between X_{zmp} and k_3.

$$k_f = (J_{pq}(q)^T)^{\#}K_q(J_{pq}(q))^{\#} \quad (8)$$

In (8), the superscript $^{\#}$ stands for the Moore-Penrose pseudo inverse. As shown in Fig. 3, the model includes only a single torsional spring through α, i.e., there is no translational spring through l. Therefore, stiffness matrix of the model solely includes k_f. K_q in (8) is the stiffness matrix of XoR, whose diagonal elements are compliant joint stiffness values (k_2, k_3). As explained in section II, hip joints do not include physical compliance, thus they are not considered in the mapping. Joint state (q) dependent $J_{pq}(q)$ is the Jacobian matrix defined between α and joint coordinates.

$$J_{pq}(q) = \begin{bmatrix} \frac{\partial \alpha}{\partial q_2} & \frac{\partial \alpha}{\partial q_3} \end{bmatrix} \quad (9)$$

The kinematic relation between α and joint coordinates can be obtained through coordinate transformation from polar to Cartesian coordinates and forward kinematics.

Given (9), solving (8) yields k_3 in terms of k_2 and k_f.

$$k_3 = \frac{k_f\left(J_{pq1}^2 + J_{pq2}^2\right)^2 - k_2J_{pq1}^2}{J_{pq2}^2} \quad (10)$$

J_{pq1} and J_{pq2} are the first and second elements of $J_{pq}(q)$ and can be computed using joint angle measurements, q. As described in section II, changes in k_2 can be estimated using the respective PAM model parameters and torque measurements [22]. Afterward, estimated k_2 can be inserted to (10), together with the desired k_f, to achieve the mapping $k_f \mapsto k_3$.

C. ZMP-based Balance Control Strategy via Ankle Stiffness

In order to distinguish the torques related to X_{zmp} and k_f, we define T_c which includes all the torque terms in (7), except the ones related to flywheel stiffness and x-axis ZMP.

$$T_c = (ml^2 + I_f)\ddot{\alpha} + 2ml\dot{l}\dot{\alpha} + b_f\dot{\alpha} - mgl\sin\alpha \quad (11)$$

A ZMP feedback scheme with a PD controller is constructed so as to introduce real-time sensory feedback for the ZMP regulation. The ZMP feedback controller output is

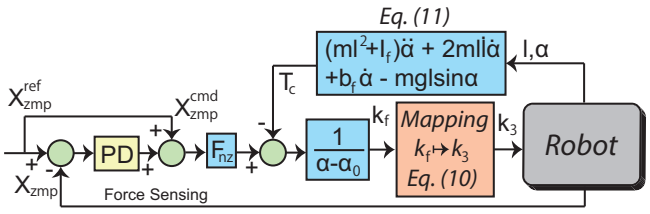

Fig. 4. ZMP-based real-time balance control scheme, in which variable ankle stiffness is utilized. Superscripts ref and cmd denote reference and command (controller output) signals. Note that position and stiffness control of PAMs [22] is not illustrated here.

defined as X_{zmp}^{cmd}. With the ZMP feedback controller in mind, the final derivation of k_f is obtained by using (7) and (11).

$$k_f = \frac{F_{nz} X_{zmp}^{cmd} - T_c}{\alpha - \alpha_0} \tag{12}$$

The control scheme is given in Fig. 4. For the implementation of this controller, T_c is computed from the actual l and α states, computed via joint angle measurements. Second derivatives are computed using approximate differentiation. F_{nz} and X_{zmp} are obtained via sensory measurement. PD gains are tuned empirically and kept the same for all experiments. Once k_f is obtained, eq. (10) is utilized to compute the corresponding k_3 trajectory. Simultaneous position and stiffness control is achieved by the method explained in [22].

IV. Experiment Results and Discussion

In order to validate the balance controller's performance, we conducted two types of experiments on our lower body exoskeleton XoR. 1) The robot is balanced using the proposed method in which variable ankle stiffness is utilized. This experiment protocol is called VAR. 2) The robot is balanced using the optimal constant stiffness value [24]. This experiment protocol is called OPT. In [24], Mosadeghzad et al. used an abstracted model that allows the computation of optimal constant ankle stiffness for bipedal robot balancing.

In both experiment protocols, the following conditions are identically met.

a) A constant standing position of $l = 0.65$ [m] and $\alpha = 4.8^o$ are input as the CoM position reference.

b) A 1.25 [m]-long pendulum with a tip mass of 4 [kg] was released towards the approximate robot CoM. The pendulum tip mass was released from an angular distance of 15^o with no initial velocity. It did hit the robot when the angular distance is around 0^o.

c) The pendulum was released 3 consecutive times. In between each release, an equal amount of delay was applied.

d) The robot is balanced in 3-D, without any tethering or supporting mechanism. It also carried a large bundle of electrical and pneumatic cables at the back on its own, without losing its balance in both cases.

The main result is displayed in Fig. 5. In these plots, solid green and purple lines depict the experiment results obtained from OPT and VAR, respectively. Yellow hatched

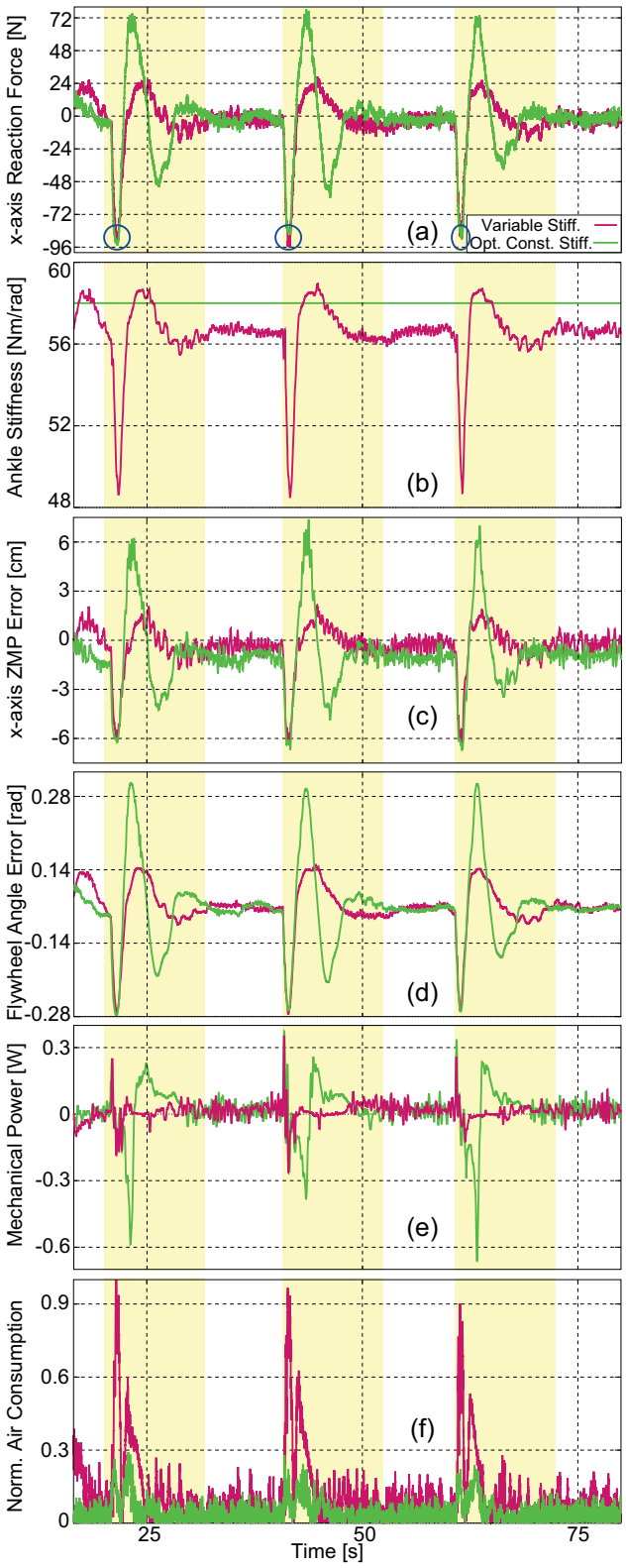

Fig. 5. Yellow hatched areas cover the periods in which the robot was perturbed and then subsequently it reacted to recover from the perturbation. a) Horizontal reaction force responses. b) Ankle stiffness variations. c) x-axis ZMP error variations. d) CoM position errors through α axis (flywheel angular deflections). e) Total mechanical power variations. f) Normalized air mass consumption plots.

areas cover the periods in which the robot was perturbed, and then subsequently it reacted to recover from the perturbation.

Horizontal reaction force responses in Fig. 5(a) indicate that the robot was perturbed in terms of equal disturbances in each experiment protocol (see the peaks indicated with circles). Right after the perturbation, the horizontal reaction force response varied between -50$\sim$75 [N], in the case of OPT. This variation was more limited in the case of VAR; it varied between $\pm$24 [N] and settled comparatively faster.

Ankle joint stiffness variations can be viewed in Fig. 5(b). In the case of OPT, the optimal constant stiffness obtained through the computation in [24] was utilized. This value is 58 [Nm/rad] for XoR. In the case of VAR, the ankle joint stiffness was varied in accordance with the balance control strategy, disclosed in section III. As the robot was perturbed by the pendulum swings, it changed between 48$\sim$58 [Nm/rad]. When undisturbed, it stayed constant around 56 [Nm/rad] which is within the vicinity of the optimal stiffness.

x-axis ZMP error variations are given in Fig. 5(c). After being perturbed, peak-to-peak x-axis ZMP error was observed to be within -4$\sim$6 [cm] for the case of OPT. This variation was 70% less for the case of VAR; it varied between -1$\sim$2 [cm]. In both experiments, the robot maintained the dynamic balance, as the ZMP error always stayed within the support polygon envelope.

Flywheel angle deflection, CoM position error in other words, is provided in Fig. 5(d). Similar to the other measurements, the α angle needed to deflect much more in the case of OPT. This is due to the fact that the constant stiffness strategy is less reactive compared to the variable stiffness strategy; the CoM needs to travel more to handle perturbations.

Total mechanical power is depicted in Fig. 5(e). For this criterion, we obtained approximately 50% decreases in peak-to-peak mechanical power measurements. As the CoM needed to travel less for the case of VAR, the required mechanical power was reduced. This appears to be an important advantage of using the variable stiffness strategy.

Fig. 5(f) displays the normalized air mass consumption. Observing this figure, we realized that we needed 70% more air mass supply for the case of VAR. This is due to the fact that simultaneous position and variable stiffness control exploits the actuator redundancy in the antagonistic setup, and demands more changes in the PAM pressure levels. Consequently, it consumes more air supply. Therefore, this appears to be the only negative result for the VAR strategy.

Fig. 6 shows a phase diagram for a single perturbation and the subsequent recovery period. It was obtained by using the experimental flywheel angle data in Fig. 5(d). After the perturbation, both strategies followed a similar trajectory up to an extent. Afterward, the variable stiffness strategy diverged and settled much faster, as the CoM followed a shorter trajectory to converge to the quiet standing state. The same convergence took a longer period for the OPT, it settled after following a longer path.

To further validate the variable stiffness strategy for various initial conditions, a series of numerical simulations are conducted. Fig. 7 illustrates the phase diagrams. As a result, the variable stiffness strategy enabled the CoM to settle faster as it followed shorter paths while converging to the quiet standing state.

Examining Fig. 4, one can see that the variable stiffness strategy utilizes a ZMP feedback strategy and it depends on the ankle joint stiffness variation in a way to minimize X_{zmp} error. The ZMP feedback controller output (X_{zmp}^{cmd}), which is obtained via the multiplication of PD block and X_{zmp} error, needs to be minimized. In this case, eq. (12) tells us that minimizing k_f, and therefore k_3, would result in minimizing X_{zmp}^{cmd}. This is why the ankle stiffness temporarily went down (see Fig. 5(d)) as the robot was perturbed, in the case of VAR.

In the case of OPT, k_3 stays constant. In order to cope with the perturbation, the angular deflection, $(\alpha - \alpha_0)$, must be relatively larger (see eq. (12)). Due to this, the CoM travels more, resulting in a longer convergence to the quiet standing state. Considering this factor, it is safe to claim that the variable stiffness strategy improves the convergence speed, and decreases CoM and ZMP errors. Consequently, it provides improved balancing characteristics compared to the optimal constant stiffness method. In exchange, it demands more air mass supply, which appears to be the price to be paid to obtain improved balancing characteristics.

V. Conclusion and Future Work

We proposed a novel real-time balance recovery method which exploits the *'variable physical'* stiffness for the first time in the literature. It combines the variable ankle stiffness property with a ZMP feedback controller, so as to achieve active balancing. Compared to the optimal constant stiffness strategy, it showed superior performance in terms of convergence speed, decreased CoM/ZMP error and reduced mechanical power requirement. Increased air mass consumption rate, on the other hand, appeared to be a limitation.

As the future work, the controller will be extended in a way so as to consider the human-robot co-existence. Changes in the human state is planned to be monitored so that the robot will react accordingly to recover from possible unbalanced situations.

Appendix

This research was supported by MEXT KAKENHI 23120004, SRPBS of the MEXT, the contract with the Ministry of Internal Affairs and Communications entitled 'Novel and innovative R&D making use of brain structures', JST-SICP, MIC-SCOPE, JSPS KAKENHI 24700203, JSPS-MIZS: Japan-Slovenia Research Cooperative Program, and ImPACT Program of Council for Science, Technology and Innovation. The authors thank N. Nakano and A. Inano for their assistance, and S. Hyon for his contribution to the initial design of the exoskeleton robot.

References

[1] M. Vukobratovic, D. Hristic, and Z. Stojiljkovic, "Development of active anthropomorphic exoskeletons," in *Medical and Biological Engineering*, vol. 12, no. 1, 1974, pp. 66-80.

[2] H. Kazerooni, "Human augmentation and exoskeleton systems in Berkeley," in *Int. Journal of Humanoid Robotics*, vol. 4, no. 3, 2007, pp. 575-605.

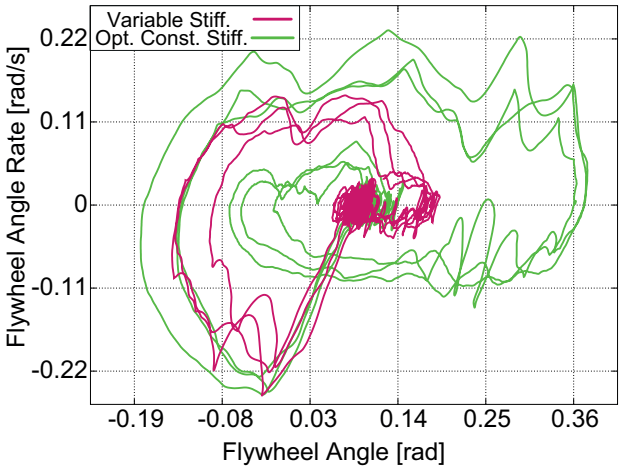

Fig. 6. Phase diagram for 3 consecutive perturbations and the related recovery periods, experiment data. The VAR strategy converges to the quiet standing state faster, compared to the OPT strategy.

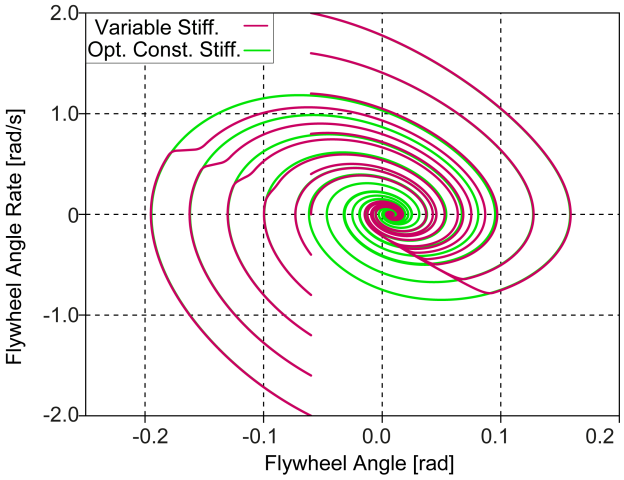

Fig. 7. Numerical simulations in which various initial conditions are given. In all trials, the VAR strategy converges to the quiet standing state faster.

[3] A. Tsukahara, R. Kawanishi, Y. Hasegawa, and Y. Sankai, "Sit-to-stand and stand-to-sit transfer support for complete paraplegic patients with robot suit HAL," in *Advanced Robotics*, vol. 24. no. 11, 2010, pp. 1615-1638.

[4] P. D. Neuhaus, J. H. Noorden, T. J. Craig, T. Torres, J. Kirschbaum and J. E. Pratt, "Design and evaluation of Mina, a robotic orthosis for paraplegics," in *Proc. IEEE Conf. on Rehabilitation Robotics*, Zurich, Switzerland, 2011, pp. 1-8.

[5] A. Esquenazi, M. Talaty, A. Packel, M. Saulino, "The ReWalk powered exoskeleton to restore ambulatory function to individuals with thoracic-level motor-complete spinal cord injury," in *American Journal of Phys. Med. Rehabil.*, vol. 91, no. 11, 2012, pp. 911-921.

[6] B. Ugurlu, H. Oshima, and T. Narikiyo, "Lower body exoskeleton-supported compliant bipedal walking for paraplegics: How to reduce upper body effort?" in *Proc. IEEE Conf. on Robotics and Automation*, Hong Kong, China, 2014, pp. 1354- 1360.

[7] N. Aghasadeghi, H. Zhao, L. J. Hargrove, A. D. Ames, E. J. Perreault, and T. Bretl, "Learning impedance controller parameters for lower-limb prostheses," in *Proc. IEEE Conf. on Intelligent Robots and Systems*, Tokyo, Japan, 2013, pp. 4268-4274.

[8] D. Sanz-Merodio, M. Cestari, J. C. Arevalo, and E. Garcia, "A lower-limb exoskeleton for gait assistance in quadriplegia," in *Proc. IEEE Conf. on Robotics and Biomimetics*, China, 2012, pp. 122-127.

[9] S. K. Banala, S. H. Kim, S. K. Agrawal, and J. P. Scholz, "Robot assisted gait training with active leg exoskeleton (ALEX)," in *IEEE Trans. on Neural Systems and Rehabilitation Engineering*, vol. 17, no. 1, 2009, pp. 2-8.

[10] J. F. Veneman, R. Kruidhof, E. E. G. Hekman, R. Ekkelenkamp, E. H. F. Van Asseldonk, and H. van der Kooij, "Design and evaluation of LOPES exoskeleton robot for interactive gait rehabilitation," in *IEEE Trans. on Neural Systems and Rehabilitation Engineering*, vol. 15, no. 3, 2007, pp. 379-386.

[11] A. M. Dollar, and H. Herr, "Lower extremity exoskeletons and active orthoses: Challenges and state-of-the-art," in *IEEE Trans. on Robotics*, vol. 24, no. 1, 2008, pp. 144-158.

[12] A. De Santis, B. Siciliano, A. De Luca, and A. Bicchi, "An atlas of physical human-robot interaction," in *Mechanism and Machine Theory*, vol. 43, no. 3, 2008, pp. 253-270.

[13] M. Zinn, O. Khatib, B. Roth, and J. K. Salisbury, "Playing it safe [human-friendly robot]," in *IEEE Robotics & Automation Magazine*, vol. 11, no. 2, 2004, pp. 12-21.

[14] N. C. Karavas, N. G. Tsagarakis, and D. G. Galdwell, "Design, modeling and control of a series elastic actuator for an assistive knee exoskeleton," in *Proc. IEEE Conf. on Biomedical Robotics and Biomechatronics*, Rome, Italy, 2012, pp. 1813-1819.

[15] M. Ishii, K. Yamamoto, and K. Hyodo, "Stand alone wearable power assist suit -Development and availability-," in *Journal of Robotics and Mechatronics*, vol. 17. no. 5, 2005, pp. 575-583.

[16] H. Yu, S. Huang, G. Chen, and N. Thankor, "Control design of a novel compliant actuator for rehabilitation robots," in *Mechatronics*, vol. 23, no. 8, 2013, pp. 1072-1083.

[17] B. Vanderborght, A. Albu-Schaeffer, A. Bicchi, E. Burdet, D. G. Caldwell, R. Carloni, M. Catalano, O. Eiberger, W. Friedl, G. Ganesh, M. Garabini, M. Grebenstein, G. Grioli, S. Haddadin, H. Hoppner, A. Jafari, M. Laffranchi, D. Lefeber, F. Petit, S. Stramigioli, N. Tsagarakis, M. Van Damme, R. Van Ham, L. C. Visser, and S. Wolf, "Variable impedance actuators: A review," in *Robotics and Autonomous Systems*, vol. 61, no. 12, 2013, pp. 1601-1614.7

[18] N. Hogan, "Adaptive control of mechanical impedance by coactivation of antagonist muscles," in *IEEE Trans. on Automatic Control*, vol. 29, no. 8, 1985, pp. 681-690.

[19] E. Burdet, R. Osu, D. Franklin, T. E. Milner, and M. Kawato, "The central nervous system stabilizes unstable dynamics by learning optimal impedance," in *Nature*, vol. 414, 2001, pp. 446-449.

[20] C. Y. Ho, and A. P. Bendrups, "Ankle reflex stiffness during unperceived perturbation of standing in elderly subjects" *The journals of gerontology. Series A, Biological sciences and medical sciences*, vol. 57, no. 9, 2002, pp. 344-350.

[21] M. Ishikawa, P. V. Komi, M. J. Grey, V. Lepola, and G. P. Bruggemann, "Muscle-tendon interaction and elastic energy usage in human walking" *Journal of Appl. Physiol.*, vol. 99, no. 2, 2005, pp. 603-608.

[22] B. Ugurlu, P. Forni, C. Doppmann, and J. Morimoto, "Stable Control Modes for Pneumatic Muscle Actuators: Force, Position and Variable Stiffness," submitted to *IEEE Trans. on Mechatronics*.

[23] S.-H. Hyon, J. Morimoto, T. Matsubara, T. Noda, and M. Kawato, "XoR: Hybrid drive exoskeleton robot that can balance," in *Proc. IEEE Conf. on Intelligent Robots and Systems*, US, 2011, pp. 2715-2722.

[24] M. Mosadeghzad, N. G. Tsagarakis, G. A. Medrano-Cerda, and D. G. Caldwell, "Power efficient balancing control for humanoids based on approximate optimal ankle compliance regulation," in *Proc. IEEE Conf. on Robotics and Automation*, China, 2014, pp. 5103-5108.

[25] C. Ott, M. A. Roa, and G. Hirzinger, "Posture and balance control for biped robots based on contact force optimization," in *Proc. IEEE Conf. on Humanoid Robotics*, Bled, Slovenia, 2011, pp. 26-32.

[26] S.-H. Hyon, "Compliant terrain adaptation for biped humanoids without measuring ground surface and contact forces," in *IEEE Trans. on Robotics*, vol. 25, no. 1, 2009, pp. 677-688.

[27] J.-Y. Kim, I.-W. Park, and J.-H. Oh, "Experimental realization of dynamic walking of the biped humanoid robot KHR-2 using zero moment point feedback and inertial measurement," in *Advanced Robotics*, vol. 20, no. 6, 2006, pp. 707-736.

[28] J. Pratt, J. Carff, S. Drakunov, and A. Goswami, "Capture point: A step toward humanoid push recovery," in *Proc. IEEE Conf. on Humanoid Robotics*, Genova, Italy, 2006, pp. 200-207.

[29] B. Ugurlu, J. A. Saglia, N. G. Tsagarakis, S. Morfey, and D. G. Caldwell, "Bipedal hopping pattern generation for passively compliant humanoids: Exploiting the resonance," in *IEEE Trans. on Industrial Electronics*, vol. 61, no. 10, 2014, pp. 5431-5443.